Electronic Supplementary Material (ESI) for Materials Horizons.

Electronic Supporting Information

General oriented assembly of uniform carbon-confined metal oxide nanodots on graphene for stable and ultrafast lithium storage

Jiashen Meng [a], Ziang Liu [a], Chaojiang Niu [a,*], Linhan Xu [b], Xuanpeng Wang [a], Qi Li [a], Xiujuan Wei [a], Wei Yang [a], Lei Huang [a], Liqiang Mai [a,c,*]

[a] State Key Laboratory of Advanced Technology for Materials Synthesis and Processing, Wuhan University of Technology, Wuhan 430070, China.

[b] Department of Physics and Collaborative Innovation Center for Optoelectronic Semiconductors and Efficient Devices, Xiamen University, Xiamen 361005, China.

[c] Department of Chemistry, University of California, Berkeley, California 94720, United States

*Email: mlq518@whut.edu.cn; niuchaojiang11@whut.edu.cn

Experimental Section

Synthesis of C@SnO$_2$@Gr

The GO was synthesized through a modified Hummer method. The solvothermal process was used to synthesize the Sn-precursor@GO with the as-prepared GO suspension (~1 mg mL^{-1}). SnCl$_2$ (0.30 g), poly(vinylpyrrolidone) (PVP, K30, 0.10 g) and 1,4-dicarboxybenzene (0.12 g) were successively dissolved in 25 mL of N, N-dimethylformamide (DMF) solvent under stirring. The resulting mixture was stirred for another 1 h at room temperature. 10 mL of as-prepared GO suspension was added into the former mixture and stirred for another 1 h. The obtained solution was transferred to a 50-mL Teflon autoclave and then heated to 160 °C for 12 h. Then, the Sn-precursor@GO was collected, washed with methanol three times and freeze-dried. Subsequently, after complete pyrolysis at 500 °C (Ramp rate: 2 °C min^{-1}) for 3 h in argon, the C@SnO$_2$@Gr was obtained.

Synthesis of SnO$_2$@C

SnCl$_2$ (0.30 g), PVP (K30, 0.10 g) and 1,4-dicarboxybenzene (0.12 g) were successively dissolved in 25 mL of DMF solvent under stirring. The resulting mixture was stirred for another 1 h at room temperature. Then, the Sn-precursor was collected, washed with methanol three times and freeze-dried. Subsequently, after complete pyrolysis at 500 °C (Ramp rate: 2 °C min^{-1}) for 3 h in argon, the SnO$_2$@C was obtained.

Synthesis of NC@SnO$_2$@Gr

SnCl$_2$ (0.30 g), PVP (K30, 0.10 g) and 2-methylimidazole (0.5 g) were successively dissolved in 25 mL of DMF under stirring. The resulting mixture was stirred for another 1 h at room temperature. 10 mL of as-prepared GO suspension was added into the former mixture and stirred for another 1 h. The obtained solution was transferred to a 50-mL Teflon autoclave and then heated to 160 °C for 12 h. Then, the Sn-precursor@GO was collected, washed with methanol three times and freeze-dried. Subsequently, after complete pyrolysis at 500 °C (Ramp rate: 2 °C min^{-1}) for 3 h in argon, the NC@SnO$_2$@Gr was obtained.

Synthesis of C@Cr$_2$O$_3$@Gr

CrCl$_3$·6H$_2$O (0.50 g), PVP (K30, 0.10 g) and 1,4-dicarboxybenzene (0.2 g) were successively dissolved in 25 mL of DMF under stirring. The resulting mixture was stirred for another 1 h at room temperature. 10 mL of as-prepared GO suspension was added into the former mixture and stirred for another 1 h. The obtained solution was transferred to a 50-mL Teflon autoclave and then heated to 160 °C for 12 h. Then, the Cr-precursor@GO was collected, washed with methanol three times and freeze-dried. Subsequently, after complete pyrolysis at 500 °C (Ramp rate: 2 °C min^{-1}) for 3 h in argon, the C@Cr_2O_3@Gr was obtained.

Synthesis of NC@Fe_3O_4@Gr

Ferric acetylacetonate (0.30 g), PVP (K30, 0.10 g) and 2-methylimidazole (0.5 g) were successively dissolved in 25 mL of DMF under stirring. The resulting mixture was stirred for another 1 h at room temperature. 10 mL of as-prepared GO suspension was added into the former mixture and stirred for another 1 h. The obtained solution was transferred to a 50-mL Teflon autoclave and then heated to 160 °C for 12 h. Then, the Fe-precursor@GO was collected, washed with methanol three times and freeze-dried. Subsequently, after complete pyrolysis at 500 °C (Ramp rate: 2 °C min^{-1}) for 3 h in argon, the NC@Fe_3O_4@Gr was obtained.

Synthesis of NC@Al_2O_3@Gr

$AlCl_3·6H_2O$ (0.30 g), PVP (K30, 0.10 g) and 2-methylimidazole (0.5 g) were successively dissolved in 25 mL of DMF under stirring. The resulting mixture was stirred for another 1 h at room temperature. 10 mL of as-prepared GO suspension was added into the former mixture and stirred for another 1 h. The obtained solution was transferred to a 50-mL Teflon autoclave and then heated to 180 °C for 12 h. Then, the Al-precursor@GO was collected, washed with methanol three times and freeze-dried. Subsequently, after complete pyrolysis at 500 °C (Ramp rate: 2 °C min^{-1}) for 3 h in argon, the NC@Al_2O_3@Gr was obtained.

Characterizations

The crystallographic characteristics of the final products were measured using a Bruker D8 Discover X-ray diffractometer equipped with a Cu Kα radiation source. SEM images were collected using a JEOL-7100F scanning electron microscope, and TEM images were collected using a JEM-2100F transmission electron microscope. Energy-dispersive X-ray spectra were recorded using an Oxford IE250 system. Raman and FTIR spectra were obtained using a

Renishaw INVIA micro-Raman spectroscopy system. The BET surface area was calculated from nitrogen adsorption isotherms collected at 77 K using a Tristar-3020 instrument. TG-DSC analysis was conducted using an STA-449F3 instrument. All solid-state NMR measurements were carried out on a 9.4 T Bruker Avance III HD NMR spectrometer equipped with a 4 mm HXY triple-resonance MAS probe at ^{1}H Larmor frequency of 400.13 MHz with the X and Y channels tuned to ^{13}C at 100.63 MHz. All NMR spectra were obtained with CP at MAS frequencies of 12 kHz for ^{13}C.

Computational details

All simulations on metal-organic frameworks were based on density functional theory (DFT) and carried out by using the projector augmented wave method (PAW) as implemented in the Vienna *ab initio* simulation package (VASP). The exchange and correlation functional was treated as generalized gradient approximation (GGA) of the Perdew-Burke-Ernzerhof (PBE) formula. The wave functions were expanded by using the plane waves up to a kinetic energy cutoff of 500 eV. Brillouin-zone integrations were approximated by using special *k*-point sampling of Monkhorst-Pack scheme with a *k*-point mesh resolution of 2π * 0.03 Å^{-1}. The unit cell lattice vectors (unit cell shape and size) and atomic coordinates were fully relaxed until the force on each atom was less than 0.02 eV Å^{-1}.

Lithium storage measurements

The anode electrodes were composed of 80 wt% C@SnO_2@Gr, 10 wt% acetylene black, and 10 wt% carboxymethyl cellulose (CMC) binder, forming a stable homogenous ink. After coating onto copper foil, the electrode film was uniformly cut into ~ 0.5 cm^{2} (area) round slices, weighing a total of ~ 1.2 mg; the corresponding areal mass loading was 2.4 mg cm^{-2}. 2,016 coin cells were assembled in a glovebox filled with pure argon gas. Lithium foil was used as the counter electrode and the separator was Celgard 2400 microporous membrane. 1 M lithium hexafluorophosphate ($LiPF_6$) solution in ethylene carbon (EC)-dimethyl carbonate (DMC) (1:1 v/v) was used as the electrolyte. The amount of electrolyte in a cell is 150 µl. Galvanostatic charge-discharge measurements were performed using a multichannel battery testing system (LAND CT2001A). CVs and electrochemical impedance spectra were collected at room temperature using an Autolab potentiostat/galvanostat.

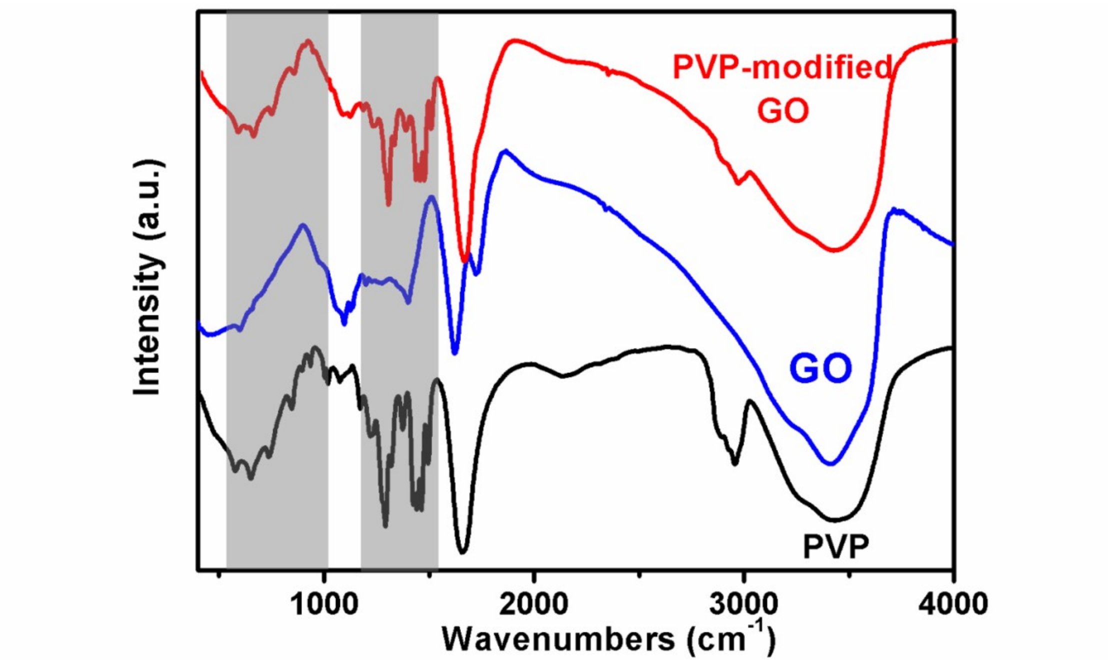

Fig. S1 FTIR spectra of PVP, GO and PVP-modified GO samples.

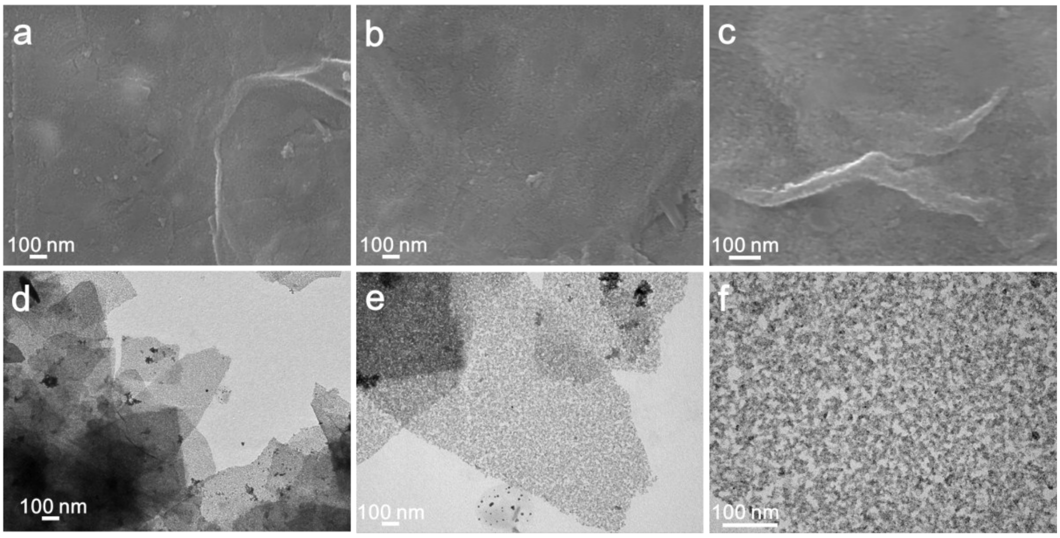

Fig. S2 (a-c) SEM images and (d-f) TEM images of Sn-precursor@GO.

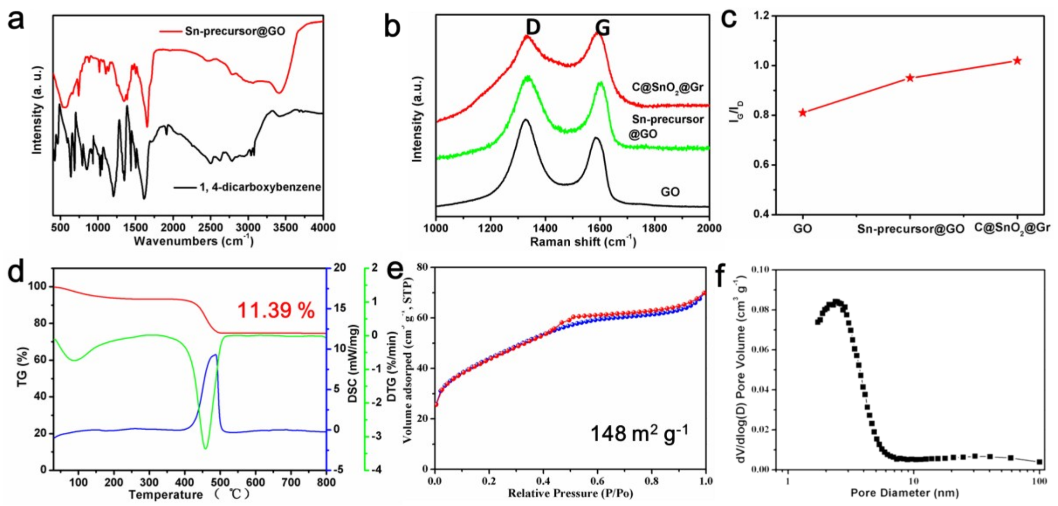

Fig. S3 (a) FTIR spectra of 1,4-dicarboxybenzene and Sn-precursor@GO. (b) Raman spectra of GO, Sn-precursor@GO and C@SnO_2@Gr. (c) The corresponding I_G/I_D ratios. (d, e) TG-DTG-DSC curves of C@SnO_2@Gr. (e) N_2 adsorption-desorption isotherms of C@SnO_2@Gr. (f) The corresponding pore size distribution.

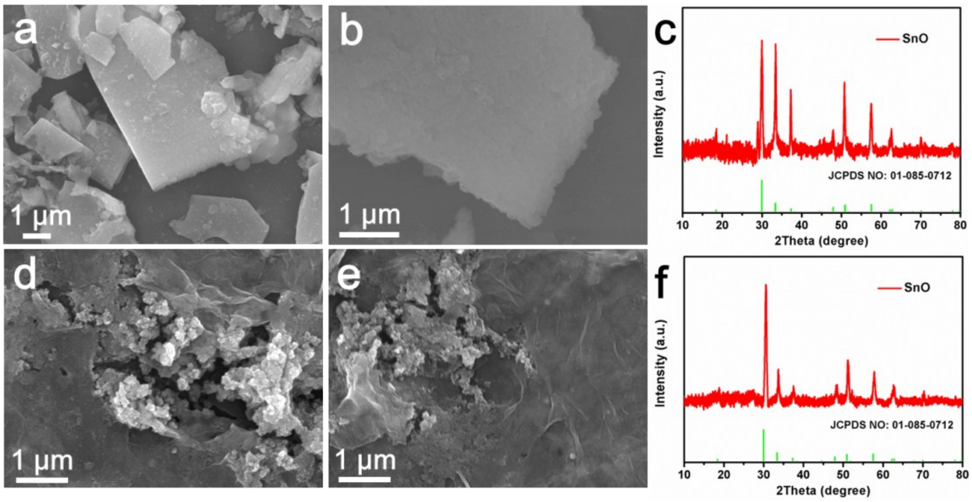

Fig. S4 (a, b) SEM images and (c) XRD pattern of SnO nanoparticles with the addition of 10 ml H_2O and without graphene oxide and 1,4-dicarboxybenzene into the reaction system. (d, e) SEM images and (f) XRD pattern of SnO/graphene oxide composite without 1,4-dicarboxybenzene into the reaction system.

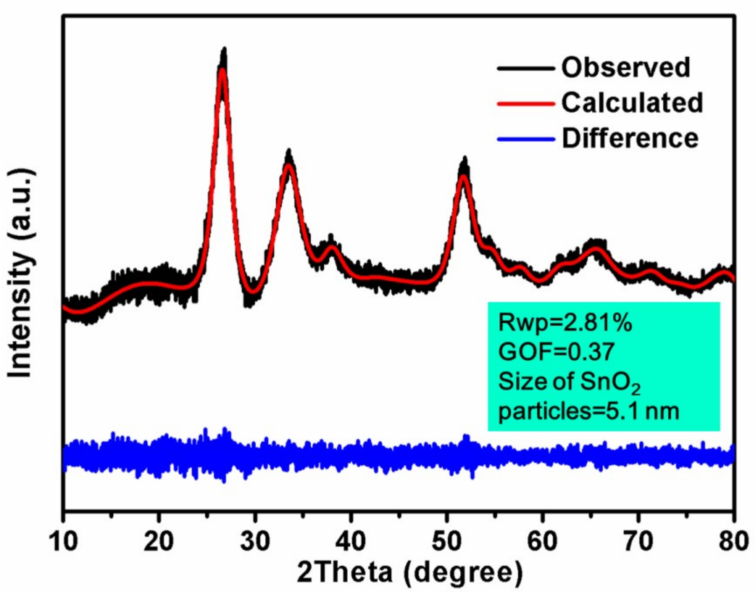

Fig. S5 Rietveld refinement analysis of C@SnO_2@Gr sample from XRD data.

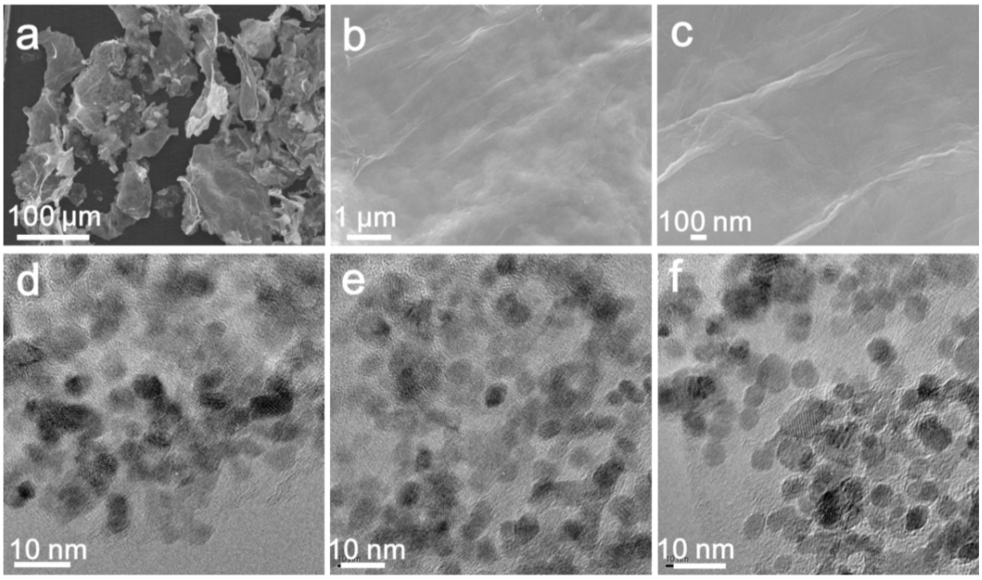

Fig. S6 (a-c) SEM images and (d-f) TEM images of C@SnO_2@Gr.

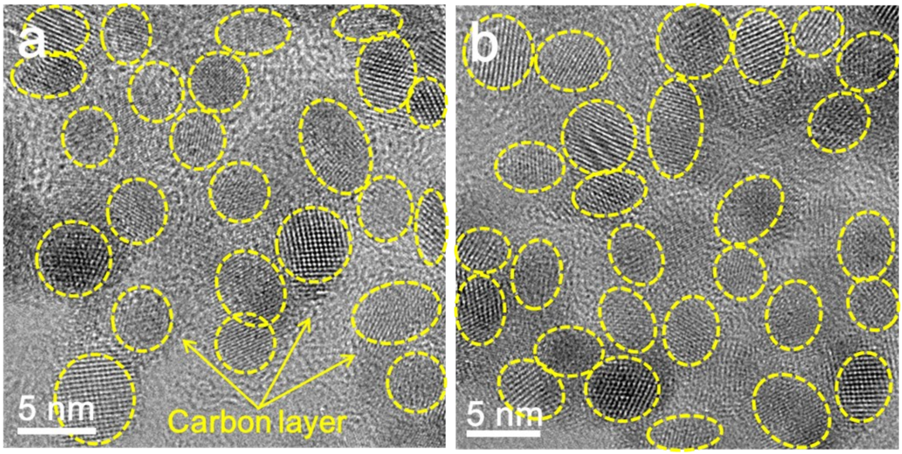

Fig. S7 (a, b) HRTEM images of C@SnO_2@Gr. The yellow circles represent SnO_2 nanodots, which are surrounded by carbon layers.

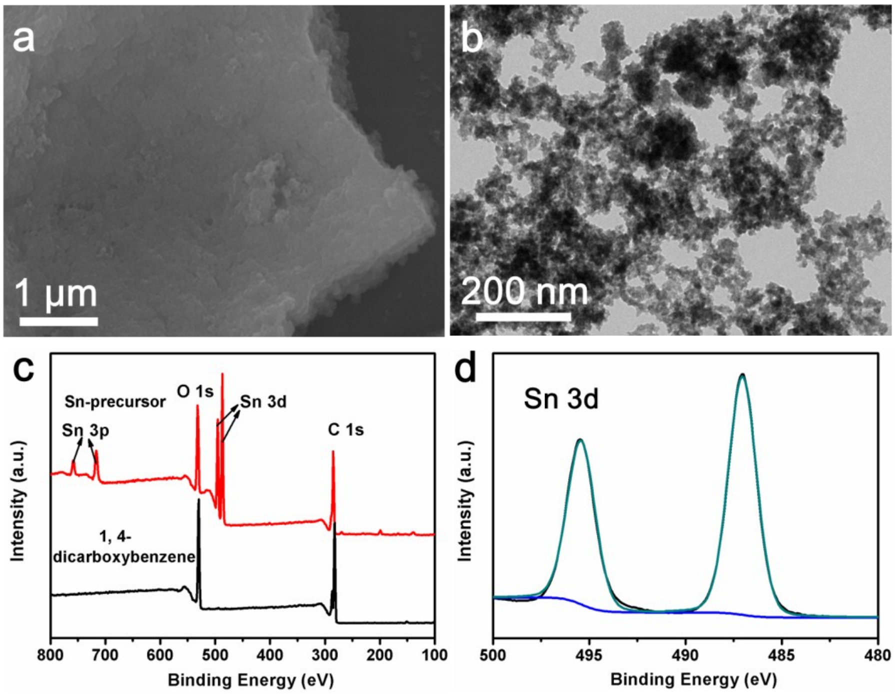

Fig. S8 (a, b) SEM and TEM image of the Sn-precursor. (c) XPS and high-resolution Sn 3d XPS spectra of the Sn-precursor.

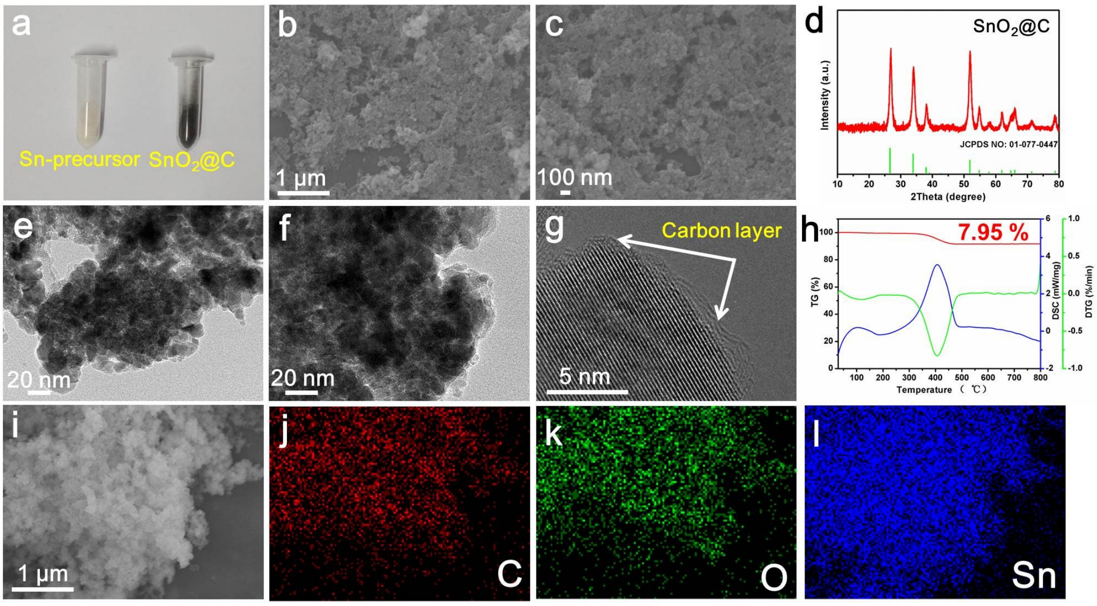

Fig. S9 (a) Optical image of Sn-precursor and SnO_2@C. (b, c) SEM images of SnO_2@C. (d) XRD pattern of SnO_2@C. (e-g) TEM images of SnO_2@C. (h) TG-DTG-DSC curves of SnO_2@C. (i-l) EDX mapping images of SnO_2@C, including the C, O and Sn elements.

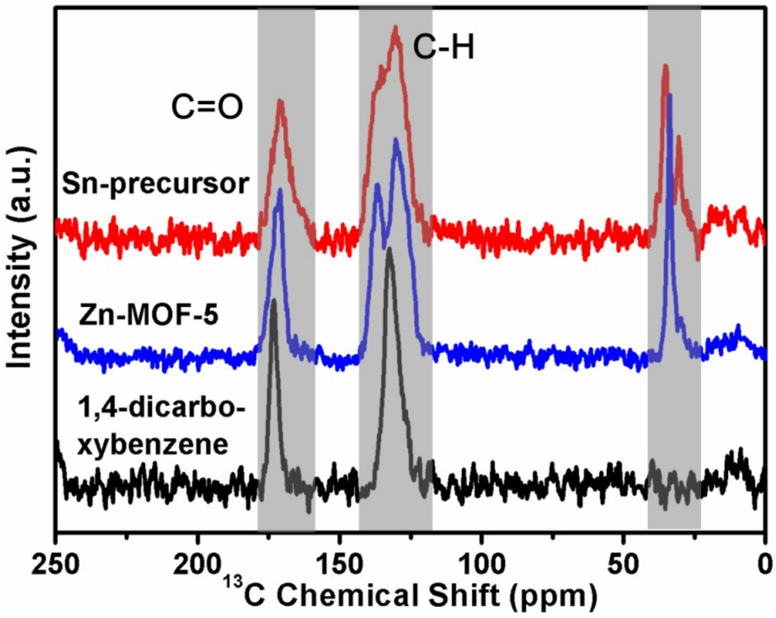

Fig. S10 ^{13}C cross-polarization (CP) magic angle spinning (MAS) solid-state NMR spectra of Sn-precursor (red line), Zn-MOF-5 (blue line) and 1,4-dicarboxybenzene (black line), respectively.

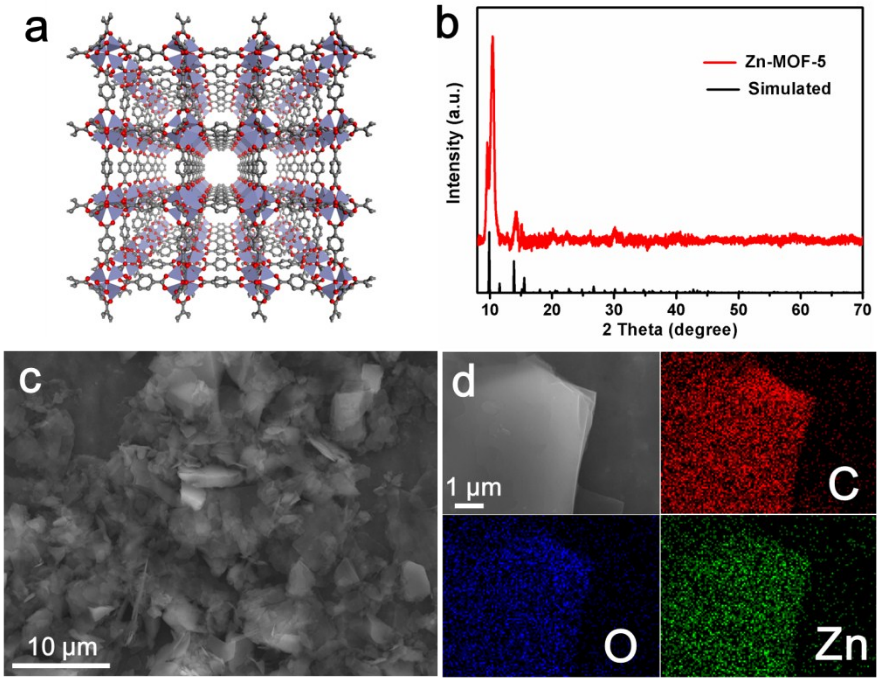

Fig. S11 (a) Crystal structure of Zn-MOF-5. (b) XRD pattern of as-prepared Zn-MOF-5 crystals. (c) SEM image of Zn-MOF-5 crystals. (d) EDX mapping images of Zn-MOF-5 crystals.

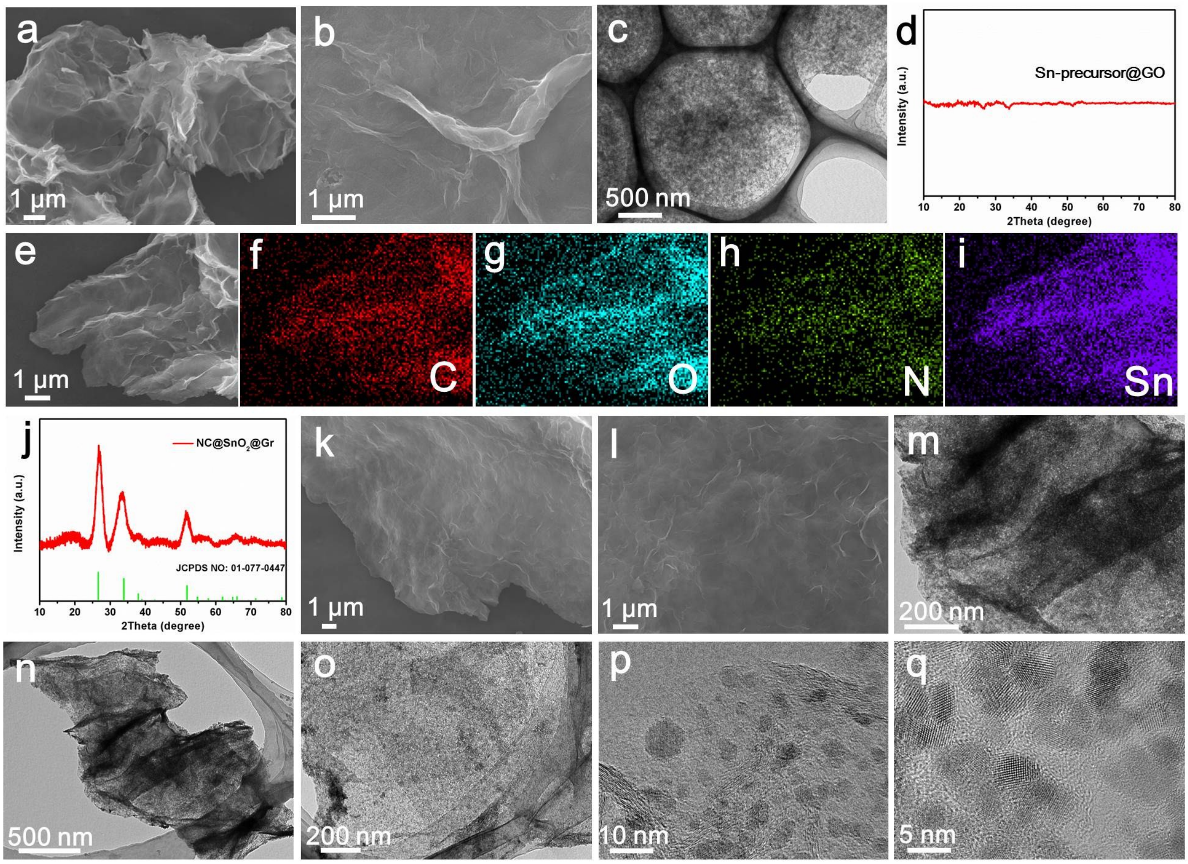

Fig. S12 SEM images (a, b), TEM image (c), XRD pattern (d) and EDX mapping images (e-i) (C, O, N and Sn elements) of the Sn-precursor@GO. XRD pattern (j), SEM images (k, l), TEM images (m-o) and HRTEM images (p, q) of the NC@SnO_2@Gr.

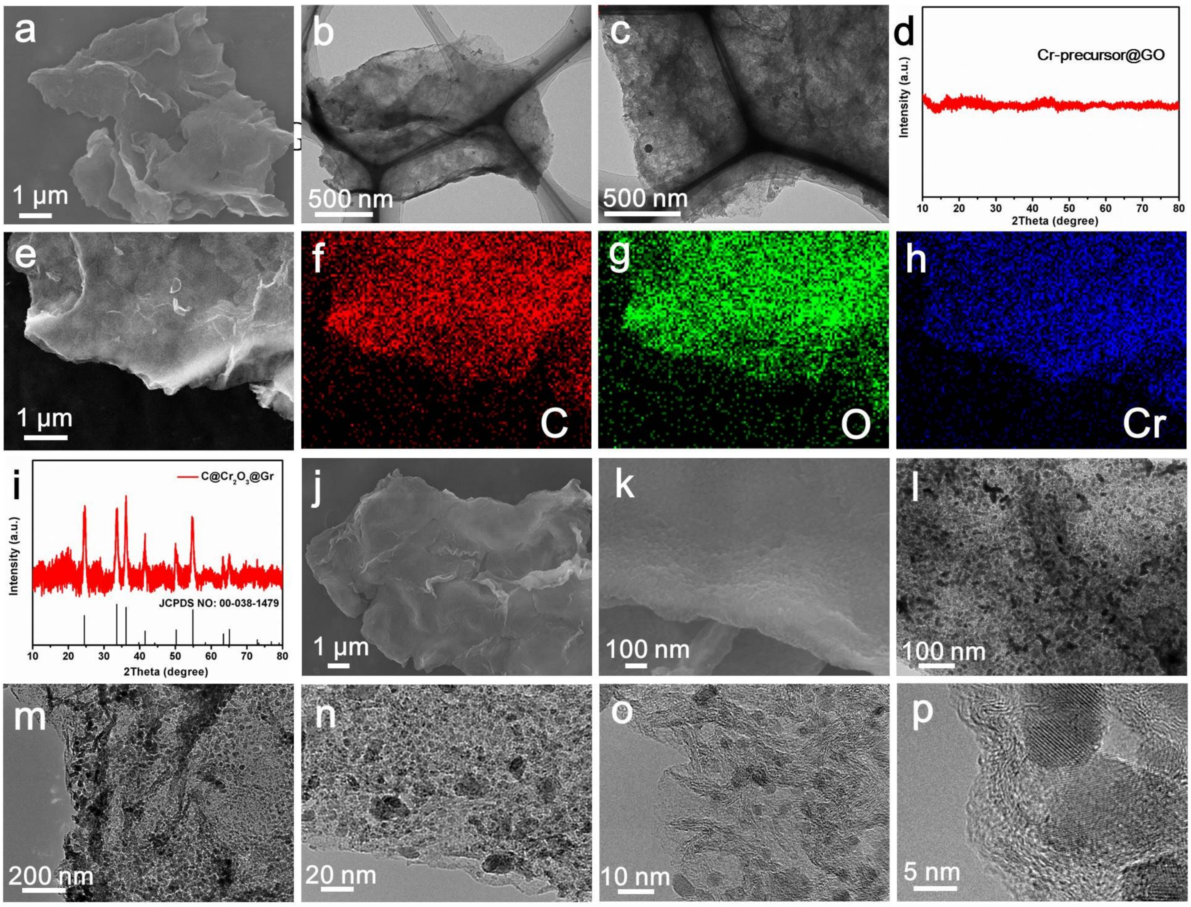

Fig. S13 SEM images (a), TEM images (b, c), XRD pattern (d) and EDX mapping images (e-h) (C, O and Cr elements) of the Cr-precursor@GO. XRD pattern (i), SEM images (j, k), TEM images (l-n) and HRTEM images (o, p) of the C@Cr_2O_3@Gr.

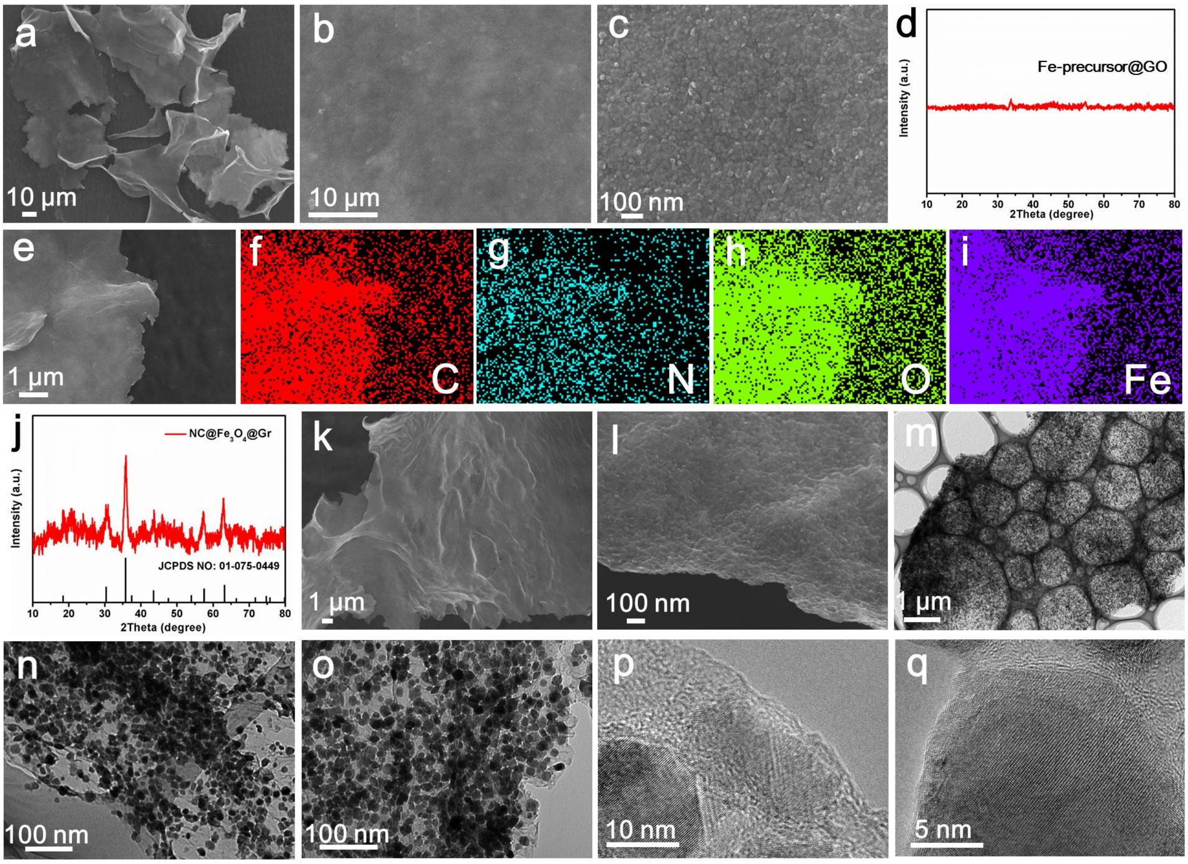

Fig. S14 SEM images (a-c), XRD pattern (d) and EDX mapping images (e-i) (C, O, N and Fe elements) of the Fe-precursor@GO. XRD pattern (j), SEM images (k, l), TEM images (m-o) and HRTEM images (p, q) of the NC@Fe_3O_4@Gr.

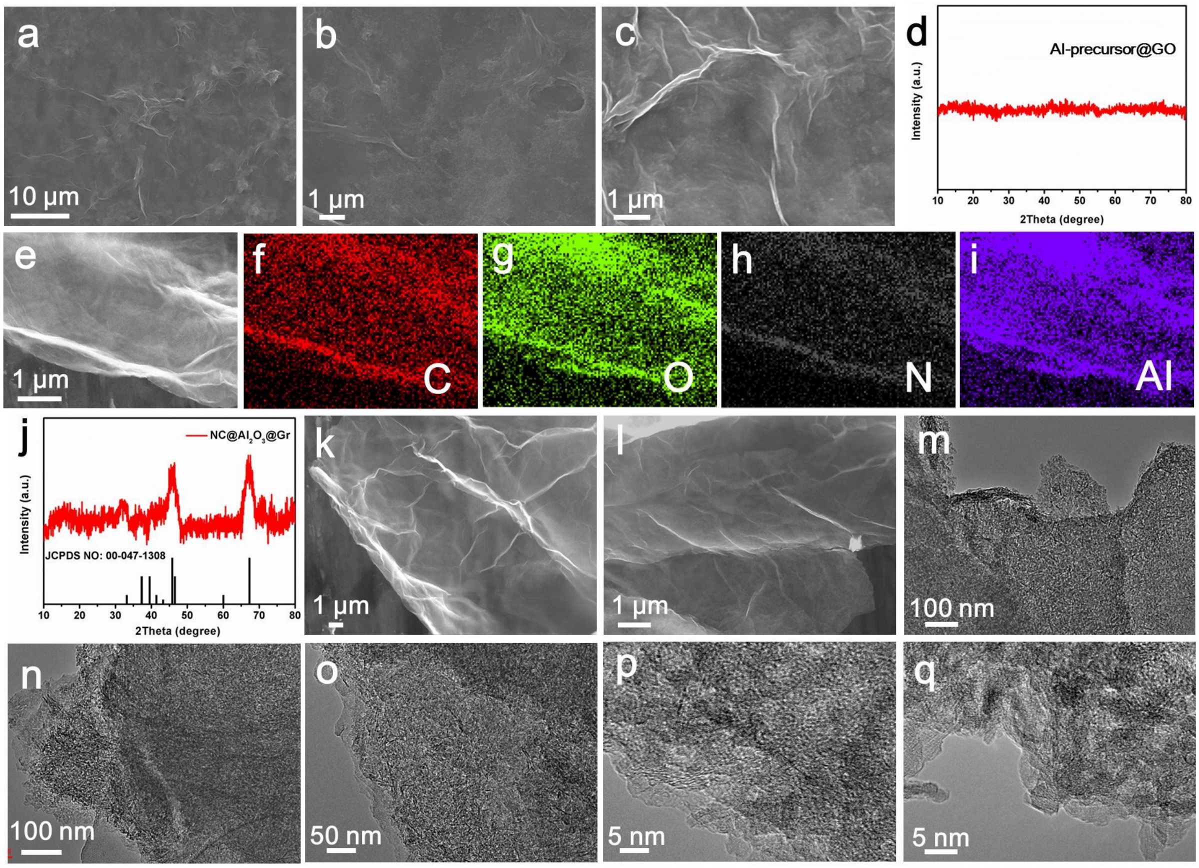

Fig. S15 SEM images (a-c), XRD pattern (d) and EDX mapping images (e-i) (C, O, N and Al elements) of the Al-precursor@GO. XRD pattern (j), SEM images (k, l), TEM images (m-o) and HRTEM images (p, q) of the NC@Al_2O_3@Gr.

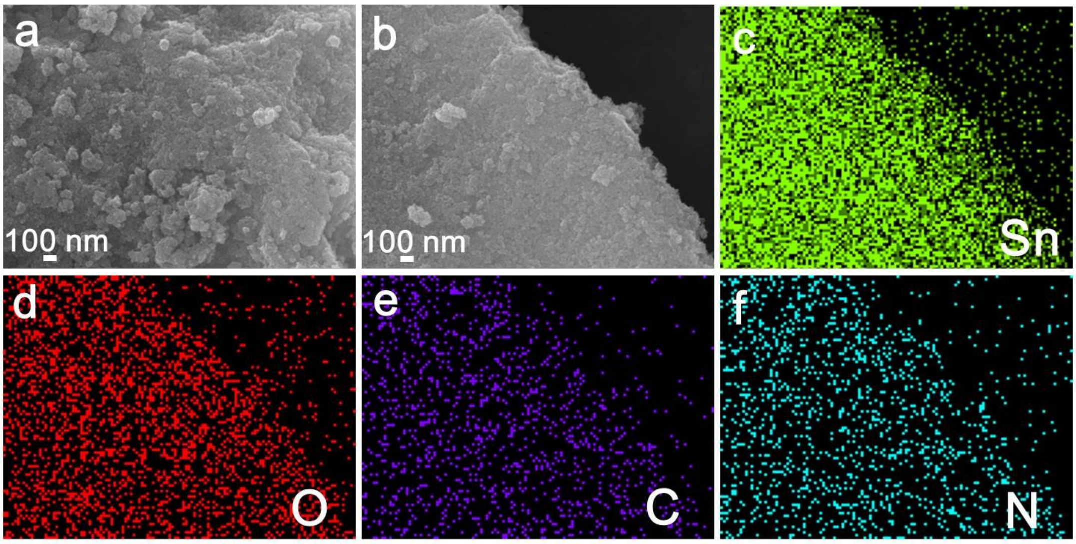

Fig. S16 (a) SEM image of SnO_2@NC nanoparticles. (b-f) EDX mapping images, including Sn, O, C and N elements.

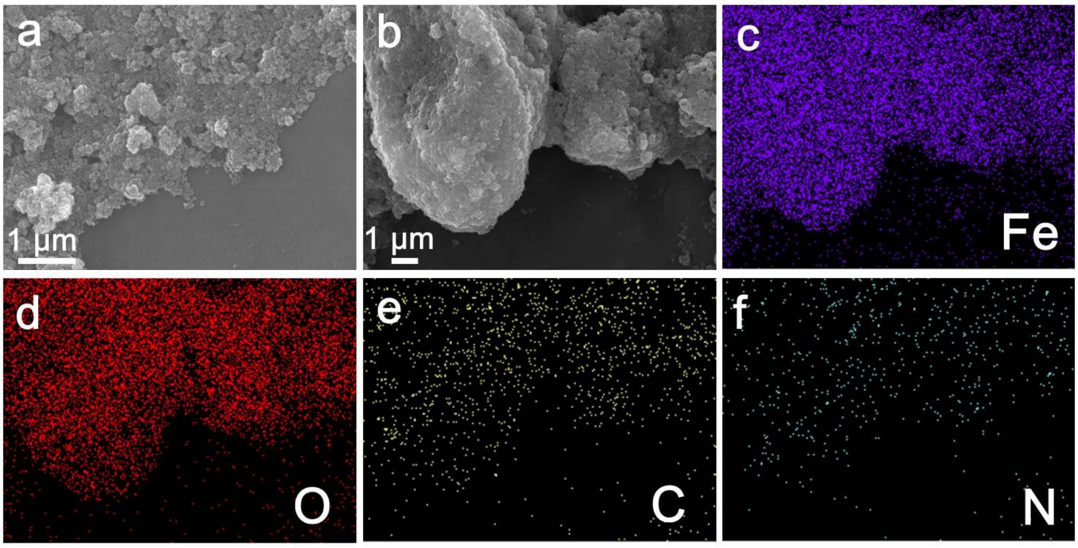

Fig. S17 (a) SEM image of Fe_3O_4@NC nanoparticles. (b-f) EDX mapping images, including Fe, O, C and N elements.

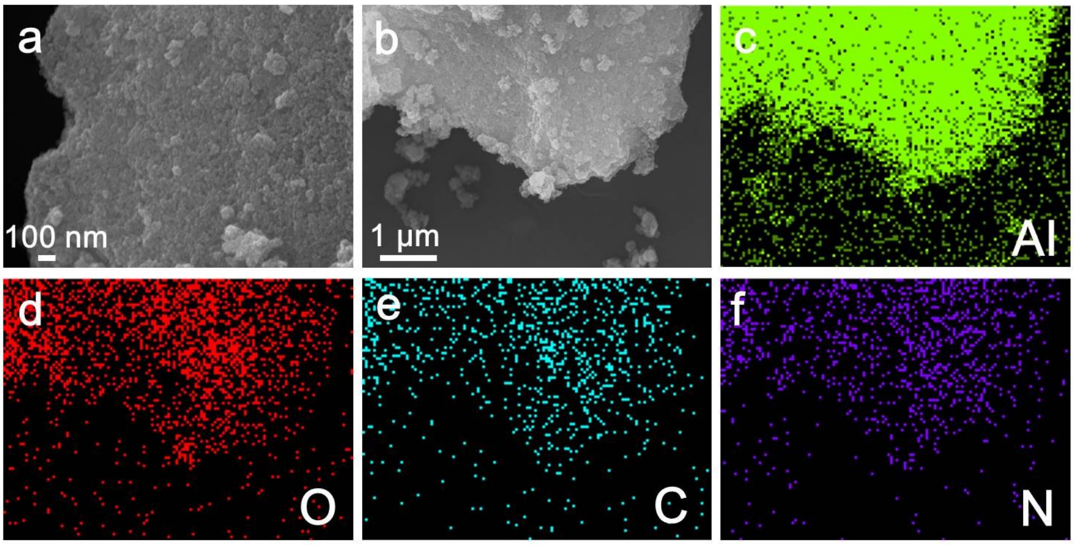

Fig. S18 (a) SEM image of Al_2O_3@NC nanoparticles. (b-f) EDX mapping images, including Al, O, C and N elements.

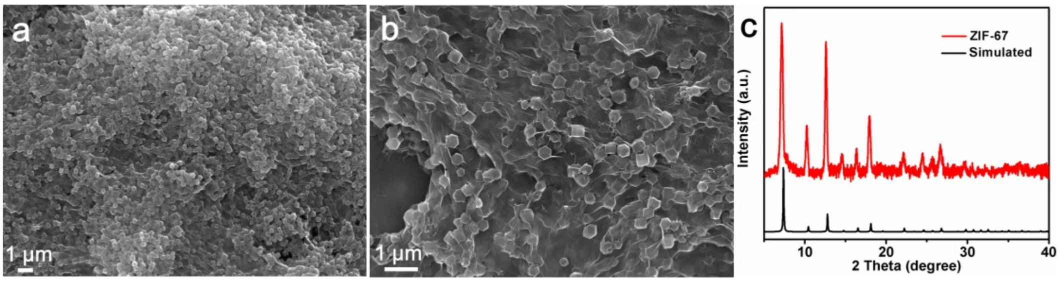

Fig. S19 (a, b) SEM images and (c) XRD pattern of ZIF67.

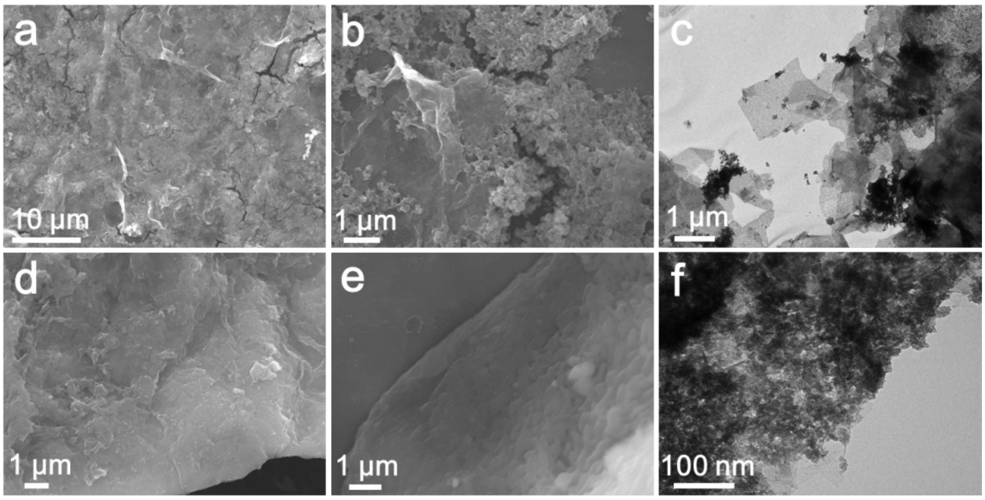

Fig. S20 (a, b) SEM images and (c) TEM image of the Sn-precursor@GO with a small amount of graphene oxides. (d, e) SEM images and (f) TEM image of the Sn-precursor@GO without the addition of PVP.

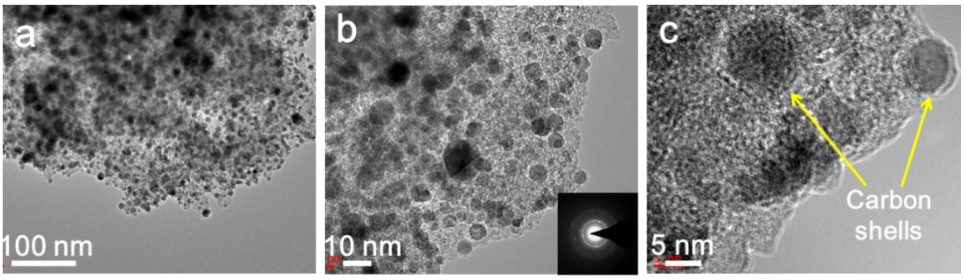

Fig. S21 (a, b) TEM image and (c) HRTEM image of C@SnO$_2$@Gr after 120 cycles at the current density of 0.2 A g^{-1}. Inset of (b) is the SAED pattern.

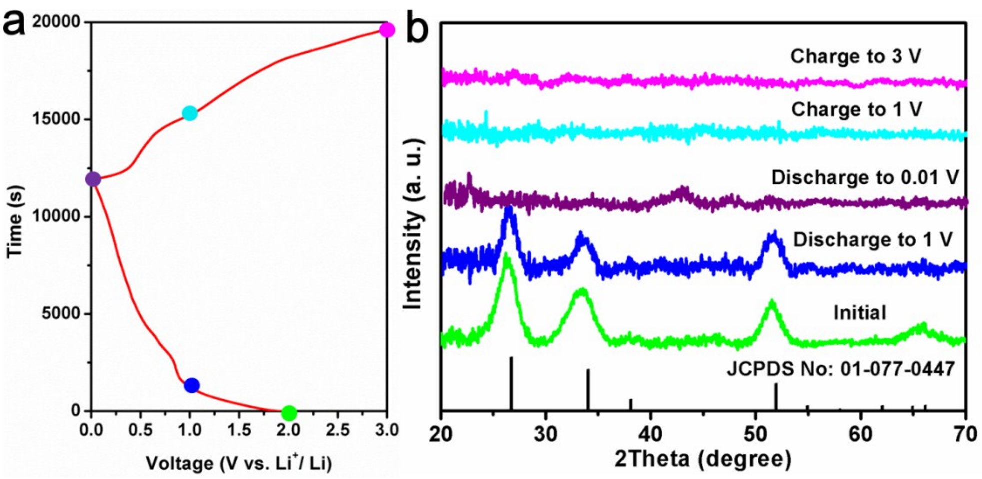

Fig. S22 (a) The initial discharge and charge process of the C@SnO_2@Gr electrode. Different color points represent different lithiation/delithiation stages. (b) The corresponding ex situ XRD patterns.

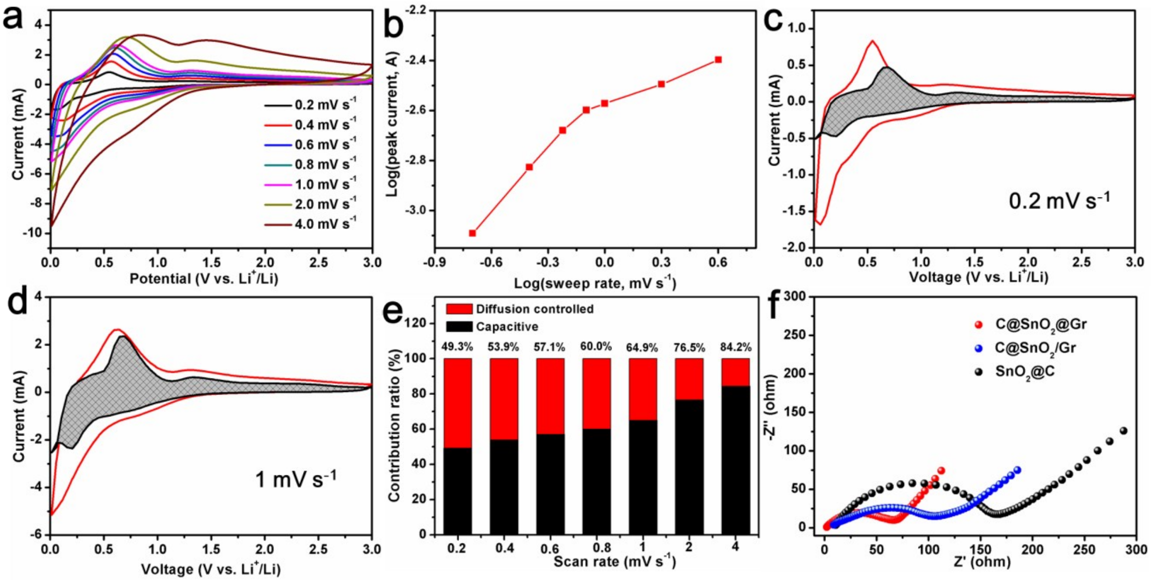

Fig. S23 (a) CV curves of the C@SnO_2@Gr at various scan rates ranging from 0.2 to 4 mV s^{-1}. (b) Determination of the b-value using the relationship between peak current and scan rate (b= ~0.86). (c, d) Separation of the capacitive and diffusion currents at scan rates of 0.2 and 1mV s^{-1}, respectively. (e) Contribution ratio of the capacitive and diffusion-controlled charge versus scan rate. (f) The Nyquist plots of the C@SnO_2@Gr , C@SnO_2/Gr and SnO_2@C samples at the first cycle.

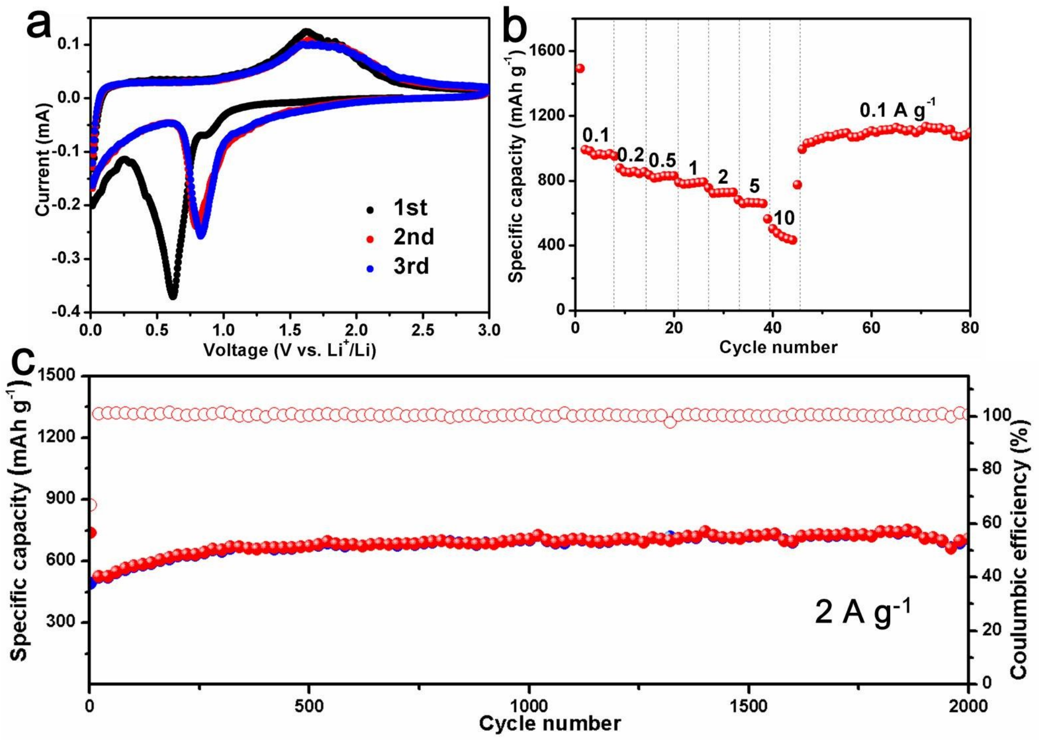

Fig. S24 Lithium storage performances of NC@Fe_3O_4@Gr. (a) The first three CV curves tested at a scan rate of 0.2 mV s^{-1}. (b) Rate performance tested at current densities varying from 0.1, 0.2, 0.5, 1, 2, 5, 10 back to 0.5 A g^{-1}. (c) Cycling performance and coulombic efficiency tested at a high current density of 2 A g^{-1}.

Table S1. Comparisons of crystal structures between Zn-MOF-5 and Sn-precursor from DFT calculations.

Crystal structures	**Bond angles**						**Distortion index**
Sn-based tetrahedron 2 (O-Sn-O)	**95.9**	**90.6**	**103.2**	**86.5**	**78.3**	**155.5**	**26.5**
Zn-based tetrahedron 2 (O-Zn-O)	**106.6**	**114.5**	**106.6**	**112.4**	**109.2**	**107.1**	**3.0**

Sn-based tetrahedron 4 (O-Sn-O)	90.0	101.7	53.9	83.6	134.7	86.9	29.8
Zn-based tetrahedron 4 (O-Zn-O)	107.3	113.1	111.6	107.3	111.0	106.2	2.6

Table S2. A comparison of our work and current main synthetic methods for graphene-metal/metal oxides hybrid materials.

Methods	Reaction principles	Products	Advantages	Disadvantages	References
Solvothermal synthesis	Mismatched coordination reaction	C@SnO_2@Gr NC@ SnO_2@Gr NC@Cr_2O_3@Gr NC@Fe_3O_4@Gr NC@Al_2O_3@Gr	● Simple manipulation ● Easy control ● Low cost ● General synthesis ● Carbon confined structure ● Uniform products	—	**Our work**
Hydrothermal synthesis	Redox reaction	SnO_2/Gr	● Simple manipulation ● Low cost	● Hard to obtain uniform products ● Hard to extend many metal oxides	*Small* **2016**, *12*, 588-594.
Elctrostatic self-assembly	Electrostatic interaction	Si/Gr	● Simple manipulation ● Low cost	● High demands for selected nanoparticles ● Weak interactions ● Hard to	*Adv. Mater.* **2015**, *27*, 1526-1532.

				obtain uniform morphologies	
Rapid thermal shock process	**High temperature**	**Si/Gr** **Sn/Gr** **Al/Gr**	**● Fast fabrication** **● General synthesis**	**● High temperature** **● High cost** **● Relatively complex manipulation**	*Nano Lett.* **2016**, *16*, 5553-5558.
High-power light irradiation approach	**Strong light**	**Pt/Gr** **Mn_3O_4/Gr** **CoO/Gr** **Fe_2O_3/Gr NiO/Gr**	**● Simple manipulation** **● General synthesis**	**● High-power light** **● High cost** **● Relatively complex device**	*Adv. Mater.* **2016**, *28*, 3305-3312.

Table S3. The comparisons of our work and previous reports on different nanostructured SnO_2 for LIBs.

Morphology	**Voltage range (V)**	**Current density (mA g^{-1})**	**Cycle number**	**Residual capacity (mAh g^{-1})**	**Capacity retention**	**Reference**
Carbon-confined SnO_2 nanodots on graphene	**0.01-3**	**200** **2000**	**120** **1200**	**1090** **702**	**104.5%** **112%**	**Our work**
Double-shelled SnO_2 yolk-shell-nanostructured microspheres	**0.01-3**	**625**	**40**	**642**	**91%**	**Ref. 39**
SnO_2@carbon coaxial hollow spheres	**0.01-3**	**500**	**100**	**460**	**79%**	**Ref. 43**
SnO_2 quantum dots on graphene oxide	**0.01-3**	**2000**	**2000**	**553**	**86%**	**Ref. 25**

Carbon-coated SnO_2 nanoplates assembled hierarchical tubular structures	**0.01-2.5**	**200**	**50**	**700**	**80%**	**Ref. 22**
Confined ultrasmall SnO_2 particles in porous carbon	**0.01-1.5**	**1400**	**2000**	**443**	**48%**	**Ref. 42**
Ordered interconnected SnO_2 nanoparticles	**0.01-1.5**	**1562**	**100**	**431**	**74%**	**Ref. 37**
N-doped carbon-coated SnO_2 submicroboxes	**0.01-3**	**500**	**100**	**491**	**52%**	**Ref. 44**
SnO_2 submicrocubes@C yolk–shell structure	**0.01-3**	**50**	**120**	**871**	**72%**	**Ref. 40**
SnO_2@TiO_2 wire-in-tube nanostructure	**0.01-3**	**400**	**1000**	**495**	**56%**	**Ref. 38**